International Journal of Heat and Mass Transfer 52 (2009) 3943–3954

Contents lists available at ScienceDirect

International Journal of Heat and Mass Transfer

journal homepage: www.elsevier.com/locate/ijhmt

Reynolds number effects within the development region of a turbulent round free jet

H. Fellouah, C.G. Ball, A. Pollard *

Department of Mechanical and Materials Engineering, Queen's University at Kingston, Ont., Canada K7L 3N6

ARTICLE INFO

Article history:
Received 3 December 2008
Accepted 23 March 2009
Available online 4 May 2009

Keywords:
Turbulent flow
Round free jet
Stationary/flying hot wire
Turbulence measurements
Mixing transition

ABSTRACT

In this work, flying and stationary hot-wire measurements were made to investigate the effect of the Reynolds number on the near- and intermediate-fields region ($0 \leqslant x/D \leqslant 25$) of a round free jet. Measurements were carried out over a range of Reynolds numbers, based on the jet exit mean velocity and the nozzle diameter, that span the mixing transition. The specific Reynolds numbers tested were 6000, 10,000 and 30,000. The objective of this study was to determine what differences there were in mean velocity profiles, turbulence intensity profiles, and velocity spectra. Results revealed a close coupling between the mean velocity distribution and the turbulence intensities and the Reynolds shear stress. From those data obtained, it was concluded that the inertial sub-range frequency span increases with distance downstream from the jet inlet and the mixing transition seems to occur at the appearance of the inertial sub-range rather than at the transition from the inertial to dissipation range.

1. Introduction

This paper owes its origins to the seminal paper by Ricou and Spalding [1], which identified that entrainment in a round jet saturated at about a Reynolds number of 20,000 and that of Dimotakis [2], which demonstrated that at this Reynolds number a transition occurs where there is a decoupling between the large scales and the viscosity dominated small scales.

Turbulent jet flows are encountered in a variety of engineering applications including combustion, chemical processes, pollutant discharge, and cooling, mixing and drying processes. Jets are also a basic building block flow that is of considerable theoretical interest. Jets have been investigated using the three pillars of scientific investigation: theory, computational simulation and/or modelling and experiment. It is now accepted that any shear flow may be characterized by coherent structures, which are of varying size and are responsible for the energy exchange between the mean flow and the turbulence, especially in the near-field region of a jet. Their evolution and interaction creates a complex three-dimensional flow field that eventually evolves to a self-similar state in the far-field. In spite of numerous experimental investigations of turbulent jet flows, many aspects of the flow remain unexplored because of the difficulty of accurately predicting the interaction of flow structures. In an AGARD report, Benocci et al. [3] concluded:

> "...*Progress in turbulence modelling and simulation has been hampered by the lack of well documented, systematically verified, experimental and numerical data bases of relatively simple building block flows for the validation of computational methods*".

This statement remains true today.

The round free jet, shown schematically in Fig. 1, is part of a large family of free shear flows, which include wakes and mixing layers. The velocity components in polar co-ordinates x, r, and θ are denoted u, v, and w, respectively. The terms in the Reynolds decomposition were denoted as $u = U + u'$, where U is the mean velocity and u' is the axial fluctuating velocity. At the nozzle, with outlet diameter D and the exit mean velocity is denoted by U_j *and* the local centreline mean velocity is denoted as U_c. The convoluted boundary in Fig. 1 represents the outer "edge" of the shear layer between the high vorticity laden jet flow and the nearly-at-rest surrounding fluid. Two common characteristic length scales have been used in the literature and represented in Fig. 1 as the jet half-radius $r_{1/2}$ determined by $U_{r1/2} = U_c/2$ and the local time-averaged diameter of the jet denoted by δ.

There are three different regions that can be defined in the axisymmetric round jet: *the near-field, the intermediate-field* and *the far-field*. The near-field region (often referred to as that region that contains the potential core) is where the flow characteristics match those of the nozzle-exit, and is usually found within $0 \leqslant x/D \leqslant 6$, Fiedler [4]. The far-field region, located at approximately $x/D \geqslant 30$, Fiedler [4], is the fully-developed or self-similar region. The intermediate-field region lies between the near- and far-fields of the jet. The near- and intermediate-fields (NIF) together comprise the development portion of the jet. The NIF often dominate practical

* Corresponding author.
E-mail addresses: fellouah@me.queensu.ca (H. Fellouah), pollard@me.queensu.ca (A. Pollard).

0017-9310/$ - see front matter © 2009 Elsevier Ltd. All rights reserved.
doi:10.1016/j.ijheatmasstransfer.2009.03.029

Nomenclature

B	decay constant, Eq. (2)
D	diameter of nozzle exit, m
E_{ii}	one dimensional spectra, Eq. (3)
f	frequency, Hz
G	acceleration due to gravity, m/s^2
R_{ii}	autocorrelation, Eq. (4)
x, r, and θ	polar co-ordinates
x_0	virtual origin, Eq. (2)
$r_{1/2}$	jet half-radius:$U_{r1/2} = U_C/2$
Re	Reynolds number
Re_D	Reynolds number at jet exit: $\mathrm{Re}_D = \frac{UD}{\nu}$
u, v, and w	velocity components, m/s
u'	fluctuating axial velocity
U	axial mean velocity
U_j	axial mean velocity at the nozzle exit
U_c	axial mean velocity at the jet centreline
U_{sled}	velocity of the probe
U_1	external or co-flow axial mean velocity

Greek symbols

δ	jet width
Δ	effective jet width, Eq. (1)

Acronyms

NIF	near- and intermediate-fields
AGARD	advisory group for aerospace research and development
DNS	direct numerical simulation
PIV	particle image velocimetry
LES	large eddy simulation
POD	proper orthogonal decomposition
EMF	electromotive motive force
LDA	laser-Doppler anemometry
SHW	stationary hot wire
CTA	constant temperature anemometer
FHWS	flying hot-wire system
rms	root mean square
RAID	redundant array of inexpensive disks
LabVIEW	laboratory virtual instrumentation engineering workbench
BNC	bayonet neill conselman

applications of a jet for which upstream conditions can significantly influence heat, mass, and momentum transfer. Therefore, the ability to control the flow development in this region would have a vital impact on many of those engineering applications mentioned above.

In the radial direction, another three regions are readily identified: *the centreline region, the shear layer* and *the outer layer*. The centreline region is where the axial mean velocity is a maximum. In the near and intermediate regions, the turbulence evolves to eventually reach equilibrium as the flow enters the far-field. In the shear layer vortex cores will form, evolve and pair-up to form large eddies because of the large velocity gradient in the radial direction. There is evidence that the vortex cores are inter-linked with longitudinal, or axial, vorticity, referred to as "braids", see, for example, McIlwain and Pollard [5]. These large eddies break down and form smaller and smaller eddies, and the turbulence structures decrease in scale (time and space). Throughout this process, energy is transferred from the large-scale structures to the smaller scales. The velocities in the outer layer are typically ~10% of U_c and of course rapidly fall to the free stream value as $r \to \infty$.

Both experimental and numerical studies, due to practical limitations, target specific regions of the jet. A comprehensive review of the myriad studies performed to date on a turbulent round jet may be found in Ball and Pollard [6]. Perhaps the beginning of modern investigations of the Reynolds number effect on round jets is Ricou and Spalding [1]. They noted that as the *Re* number increased from about 20,000 and beyond, the entrainment in the jet was constant. Subsequently, various other studies have examined other features and regions of the round jet. The far-field of the jet has been well studied (Wygnanski and Fiedler [7], Rodi [8], George [9], Dowling and Dimotakis [10], Panchapakesan and Lumley [11], Richards and Pitts [12], Hussein et al. [13], Uddin and Pollard [14]). In spite of the large number of studies dedicated to the far-field, there are conflicting results regarding the existence of universal self similarity. Dowling and Dimotakis [10], Pitts [15], Richards and Pitts [12] and Antonia and Zhao [16] support the hypothesis of universal self-similarity. They showed that the self similar-region has minimal dependence on initial conditions. In the other words, the asymptotic growth rates of all jets are universal and the asymptotic normalized scalar fields of all jets are identical, regardless of jet initial conditions. Other studies claim that the self-similar region is not universal, citing its dependence on the initial conditions, especially George [9]. Boersma et al. [17] performed a direct numerical simulation (DNS) of a round jet. They found that different nozzle outlet conditions affect the mean and fluctuating velocities. Ferdman et al. [18] experimentally considered the effects of non-uniform initial-velocity profiles on the downstream evolution of round turbulent jets over $0 \leqslant x/D \leqslant 80$. They found that the evolution of both jets, one with an axisymmetric fully developed inlet profile and the other with an asymmetric initial profile, evolved toward a self-preserving state more rapidly than that of a jet with a top-hat initial velocity distribution although the initial growth in the turbulence quantities is higher for a uniform inlet condition. On the other hand, the initial growth of turbulence intensities and the far-field decay rates were larger for the jets with uniform initial-velocity profiles. Mi et al. [19] examined experimentally the jet flow field over $0 \leqslant x/D \leqslant 40$, using three types of axisymmetric nozzle. They showed that the differences in mixing rates were associated with different underlying turbulent structures. Romano and Antonia [20] used two round jets with slightly different initial conditions, and hence different ratios of the longitudinal to transverse rms velocities, found that the difference between scaling exponents of longitudinal and transverse velocity structure functions in the far-field were dependent on the anisotropy of the flow. Matsuda and Sakakibara [21] used a stereo particle image velocimetry (stereo-PIV) system to visualise turbulent vortical structures ($20 \leqslant x/D \leqslant 50$) over a Reynolds number range of Re_D = 1500–5000, based on the nozzle exit condition. In

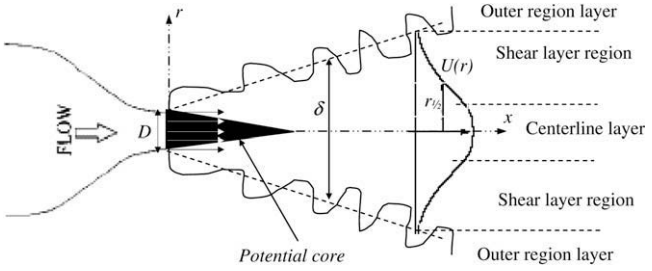

Fig. 1. Schematic of the round free jet and coordinate system.

this Reynolds number range and in the region considered, there was a Reynolds number dependence on the shear stress distributions. Flow visualisation showed hairpin vortices and vortex strings. The typical spacing between the legs of the hairpin was independent of the Reynolds number.

The analytical results of George [9] showed that the difference between jet experimental data found in the literature may not be solely due to experimental errors, but may be attributed to incorrect scaling. He concluded that a variety of self-similar states are possible depending on the initial conditions. In a comparative review of several different studies on turbulent jets and plumes, Carazzo et al. [22] proposed that, in an appropriate parameter space for entrainment, global evolution toward self-similarity follows a universal route. They defined an *entrainment coefficient*, which is a function of the Reynolds-averaged profiles that depend on velocity, buoyancy, and the turbulent stresses. The formulation of this coefficient permits a quantitative description of the evolution of self-similarity. More recently Uddin and Pollard [14] used large eddy simulation (LES) to investigate the effects of initial conditions on a weakly co-flowing jet (inner to outer axial mean velocity ratio = 11:1). They confirmed that the self-similar state is achievable with prudent choices of length and velocity scales, and of virtual origin. The commonly used scales, the half-value distance or the jet half radius, are not physically relevant. To overcome this limitation, they proposed a new scale: *the effective jet width* Δ. This scale is based on Townsend's variance in the velocity distribution and is defined by:

$$\Delta^2 = \frac{\int (U - U_1) r^2 dr}{\int (U - U_1) dr} \tag{1}$$

where U_1 is the external or co-flow velocity and for a free jet, $U_1 = 0$. It is a kinematic length scale and reflects the effect of the formation of the viscous layer at the orifice exit.

In the near- and intermediate-fields, the flow dependence on the initial conditions is clearer. Hussain and Zaman [23] employed controlled excitation in order to improve deduction of coherent structures in the near-field ($x/D \leqslant 14$) of a round jet for Reynolds number Re_D = 25,000–110,000. It was found that while the preferred-mode coherent structures were independent of the nature of the initial shear layer (laminar or turbulent), the size and orientation of the structures were also Reynolds number dependent. Radial momentum transport was found to be affected by the coherent structures.

Olsson and Fuchs [24] conducted an LES on the near-field region ($0 \leqslant x/D \leqslant 9$) of a round jet. Simulations were performed for three Reynolds numbers, Re_D = 10,000, 50,000 and 500,000. The decay rate of the mean streamwise centreline velocity at lower Reynolds number was found to coincide with higher levels of turbulence intensity. Mcllwain and Pollard [5] simulated the near-field of round jets both with and without swirl. Ring structures, which were aligned with the plane normal to the flow form in the jet shear layer and they were linked to successive ring structures by streamwise braid structures. The resulting interaction causes the rings to break apart into smaller, less organized turbulence structures and swirl enhanced this breakup. Entrainment into the jet increased as a result of the addition of swirl and this was traced to increased occurrence of streamwise braids.

Jung et al. [25] considered the near-field ($0 \leqslant x/D \leqslant 6$) and structures were observed to have strong dependence on streamwise position. The reconstruction of the full-field streamwise velocity component using the dominant proper orthogonal decomposition (POD) modes clearly showed the evolution of the flow with downstream position, from 'volcano-type' eruptions at two to three diameters downstream to a 'propeller-like' blade pattern where the number of blades diminish with increased downstream distance.

Burattini et al. [26] examined the modification of the initial development of the jet through the introduction of different grids at the exit plane of the jet. As a consequence of weaker coherent structures, which are less capable of entraining quiescent fluid from the surroundings, their jets showed a decreased radial growth rate and an extended region of streamwise decay with a concomitant lengthening of the potential core.

For a Reynolds number range, Re_D = 177–5142, and for a region extending from the near to the far-field, Kwon and Seo [27] used PIV to report the Reynolds number dependence on several turbulence statistics. They found that as the Reynolds number increased the length of the near-field region decreased, the centreline velocity decayed more rapidly, the spreading rate for the turbulent flow cases decreased gradually, the normalized turbulence intensity along the centreline increased more rapidly with axial distance and the Reynolds shear stress level increased.

Bogey and Bailly [28] studied the Reynolds number effects, Re_D = 1700–400,000, on transitional round jets ($0 \leqslant x/D \leqslant 20$) using large eddy simulation (LES). Reynolds number variations were shown to have a significant effect on development of the jet mean flow and turbulence statistics, both in the shear layer and the transitional region just downstream from the potential core. With lower Reynolds numbers, higher turbulence intensities, and larger integral scales, more rapid development of the jets was observed. The energy dissipation was shown to depend closely on the Reynolds number.

Thirty nine years after Ricou and Spalding [1], Dimotakis [2] proposed that their observation that the entrainment saturates beyond $Re \sim 20{,}000$, may be traced not to the large-scale structures in the flow, which are peculiar to the geometry considered, but rather to the physical significance of the various scales of the turbulence and Reynolds number scaling. Dimotakis demonstrated there is a decoupling between the large scales and those free from the effects of viscosity. That is, there is a "viscous decoupling of the outer and inner scales of turbulence as responsible for the transition criterion"; however, the relative magnitude of these length scales, while important, do not provide the linkage to the observed effects of initial conditions on the flow. Moreover, to the present authors' knowledge, a systematic investigation that spans the transitional Reynolds number range suggested by Dimotakis [2] of a turbulent jet has not been undertaken.

In this paper, the near- and intermediate-fields of a free round jet for a Reynolds number range that spans the mixing transition is considered, that is $6000 \leqslant Re_D \leqslant 30{,}000$. The objective was to better understand the turbulent flow development and the evolution toward the self similarity. The region under consideration spans the near- and intermediate-fields, $0 \leqslant x/D \leqslant 25$. As important, this paper provides the first results from the application of a novel flying hot-wire apparatus and it is demonstrated that the experimental methodology, including the data reduction schema, applied to the flying hot-wire data match those obtained for a stationary hot wire.

The rest of the paper is organized as follows. The next section of this paper provides details of the experimental set-up and data processing. Results obtained will be presented and discussed in the third section. Finally, the conclusions drawn are provided in the fourth section.

2. Experimental set up

2.1. The flying hot-wire system (FHWS)

There is a large body of experimental data in the archival literature obtained using stationary hot-wire probes; however, these data have inherent limitations. For example, stationary probes

suffer from directional ambiguity due to cross-flow, rectification, and drop-out errors, all of which increase with increased turbulence intensity. Beuther et al. [29], Panchapakesan and Lumley [11] and Hussein et al. [13] observed significant differences between laser-Doppler anemometry (LDA) and stationary hot-wire (SHW) measurements, especially in the higher-order moments. They showed that the SHW results confirmed substantial deviations that were consistent with the hot-wire errors. The LDA and flying hot-wire (FHW) results, on the other hand, were confirmed to be consistent with the equations of motion and momentum.

To avoid stationary hot-wire errors, the effective turbulence intensity that is measured by the probes should be reduced. This can be accomplished by using a flying hot-wire system in which the probes are moved through the fluid at a velocity greater than the maximum possible backflow velocity. With sufficiently high speed of the probe, those data obtained will not have biases as in case of SHW data. This point cannot be overstated: the field of experimental turbulence research has matured to the point where the next generation of students, and the broader fluid mechanics community, seek greater fidelity in those data taken within a particular flow especially with the maturation in computational fluid dynamics and direct numerical simulation of turbulence. The first FHW system was developed by Cantwell [30] where the hot-wire probe followed a circular path. Watmuff et al. [31] considered a linear horizontal path for the hot wire, Thompson and Whitelaw [32] considered a curvilinear motion and Panchapakesan and Lumley [11] considered a linear vertical path for their hot-wire probe. Some advantages of using a flying hot-wire system over a stationary wire were given by Hussein et al. [13] and Cole and Glauser [33]: "by superimposing a velocity on the hot wire, the effective turbulence intensity, given by $u'/(U + U_{sled})$, where U_{sled} is the velocity of the probe, was reduced and thus the errors as well as the effect of the fluctuating convection velocity on the measured derivative was reduced. With the probe velocity, U_{sled}, sufficiently high, rectifications were avoided by keeping the relative velocity in one direction. The imposed probe velocity reduces the cone angle of the velocity vectors relative to the cross-wire probe and then the simplifying assumptions used for cross-wire calibrations become more applicable. The moving hot wire improves the approximation of Taylor's frozen field hypothesis, Cole and Glauser [33], since the turbulence intensity was reduced. Finally, by "flying" the probe through still ambient fluid, low speed calibrations can be obtained".

In the current experiment, single and X-wires, which were made of tungsten wire 5 μm in diameter and 1 mm in length (Auspex Corporation), were mounted on a 1 m long aerodynamic sting (Fig. 2) the cross section of which was designed to minimise air drag. The probes were mounted approximately 0.1 m away from

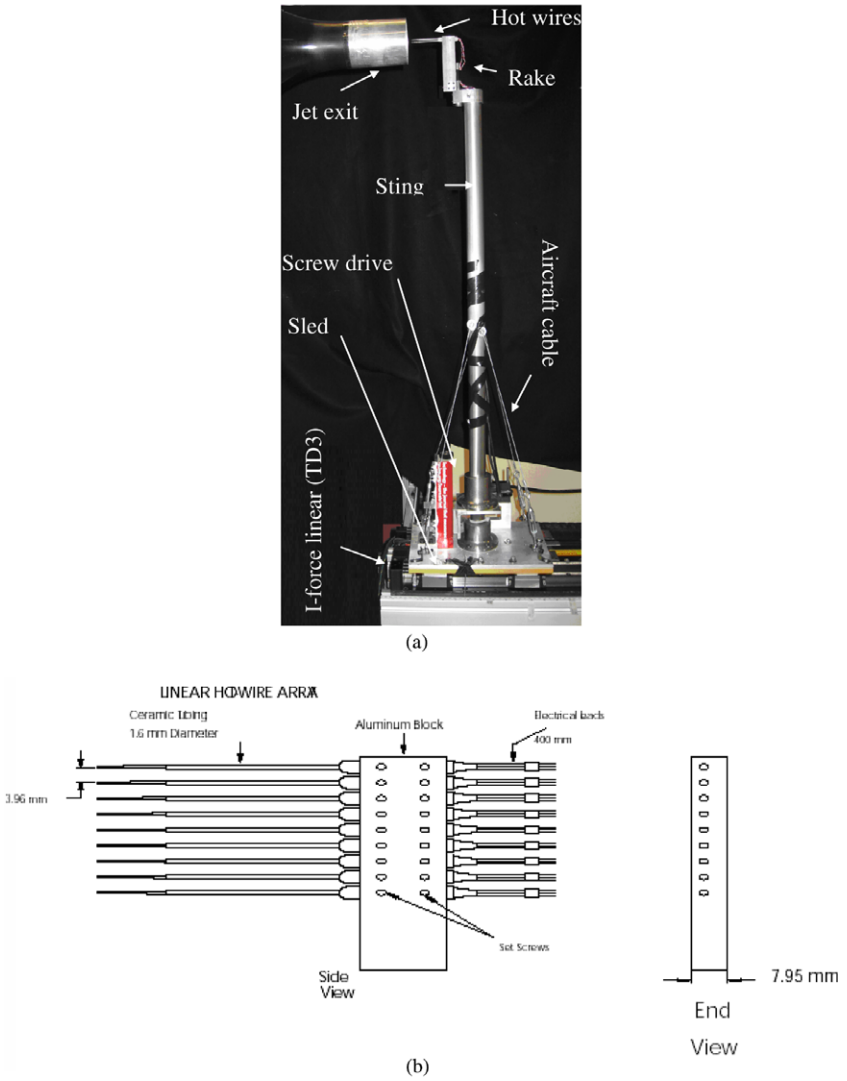

Fig. 2. Sting and hot-wire rake: (a) the sting; (b) the rake. In the current experiments, only one probe was used.

the tip of the rake to minimise interference. To avoid vibrations of the sting, it was fixed to the sled with four aircraft-cables. The system (hot wire, rake and sting) was driven by a linear motor system in the x-axis direction. The linear motor used is the Parker-Trilogy I-force ironless unit (model: TD3) with 3 m of travel. It can accelerate the sled, sting, and rake assembly (estimated at 9 kg, Fig. 2) to ~3 m/s, which imposes 7G on the wires where G is the acceleration due to gravity. This linear motor was chosen for its many advantages: high speeds, high accelerations, faster response (100 times that of a mechanical system), high precision due to an in-built positioning encoder and long travel without performance loss. Ironless motors, also known as "*U-channel*" motors, consist of a forcer that rides between dual magnet rails. The forcer does not have any iron laminations in the coil – hence the name ironless. Instead, the copper windings are encapsulated and located in the air gap between the two rows of magnets. Because the motors are ironless, there are no attractive forces or cogging forces between the forcer and the magnet track. To use the FHW with confidence, the velocity of the sled must be at least equal to back-flow velocities that are on the order of 30% of mean flow velocity, Hussein et al. [13]. Fig. 3 illustrates the mean velocity of the sled as it was "flown" through still ambient fluid (the jet was not operating). The velocity of the sled was measured using a calibrated single-wire probe and the results were averaged over 20 runs. It has a trapezoidal profile: the sled was accelerated within 6D to a maximum velocity of 3 ± 0.05 m/s and then decelerated to rest within 4D. The distance the sled traveled at a constant velocity was 19D. Both the acceleration and deceleration time and length can be altered; however, those given were deemed to be adequate for this study. The velocity of the sled, as determined by a built-in encoder that was linked to the data acquisition system, was confirmed using a digital video recorder. The encoded record of instantaneous sled/probe velocity was later subtracted from those data taken during a measurement campaign on the jet. The humps seen in the average profile (Fig. 3) are a result of the drive overshooting and undershooting the desired constant velocity. These extrema were not of concern because the difference between runs was undetectable and the actual velocity was known from the encoder signal. The sled traverse was aligned with respect to the jet's axis before each experiment so that the vertex of the probe rake was located at the centre of the nozzle during its entire downstream displacement; this was confirmed by placing a graph-sheet (mm grid sheet) mounted on the nozzle outlet plane and a laser pointer was mounted on the rake. The sled was moved downstream to make sure that the laser-pointer beam on the graph-sheet did not move. The hot-wire signal was transmitted from the probes to the anemometer using a coaxial cable. To avoid vibrations vie the probe–cable connection, the coaxial cable was fixed to the bottom of the sting and then passed through pulleys that run on a taught cable located at the outer edge of the FHWS support frame and parallel to the jet axis. The movement of the probe in the spanwise y-direction was performed by a belt-drive positioner (Parker-Trilogy HPLA Linear actuator model HPLA080). In the z-direction (vertical), the location of the rake was controlled by a screw drive. The resolution of the motion in three directions was estimated to be 0.05 mm. The base of the FHWS, shown on Fig. 4, was designed to be stationary to minimise vibrations in the system through direct coupling with steel I-beams and the laboratory floor. The whole system provides precise linear motion in three directions.

2.2. The jet

Air was generated by a fan, which was mounted on anti-vibration pads, was powered by an electric motor and controlled by a variable frequency electronic drive (model: *GP2000 A-C-VS*). The air was then sent to a settling chamber through a neoprene duct, which was designed to reduce the transmission of vibrations generated by the fan. The settling chamber consists of a filter, a flow straightening section made of drinking straws, and three screens with different porosities. The purpose of the settling chamber was to break up any large-scale structures and reduce the overall turbulence intensity. Air exits via a round duct to the inlet of the nozzle with an exit diameter $D = 8.25$ cm. There are different types of nozzles used in the literature: smoothly contracting, long pipes, and orifice plates. To produce a uniform velocity distribution (top-hat velocity profile) over a short length, a smoothly contracting nozzle with the exit contraction was constructed using a fifth order polynomial, Morel [34]. The end of the nozzle had affixed to it a tapered nozzle piece that ends with a razor-sharp end (land thickness 0.05 mm) see Fig. 5; this design was chosen to assist those who may wish to simulate the experimental configuration and thus there should not be any confusion about the exit land thickness. The exit plane of the flow (the region behind the jet exit plane) was open so that entrainment into the jet may occur both laterally (in the radial direction) as well as from behind the jet exit plane. The apparatus was situated in a large room; however, as was noted above, irrespective of the size of the room, entrainment and jet development will be affected by the experimental (boundary)

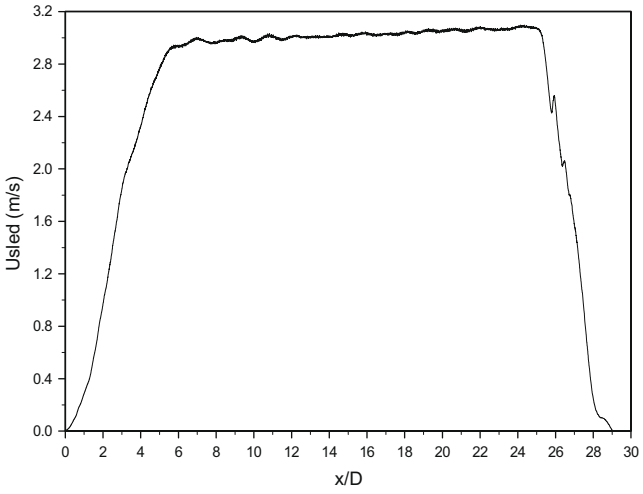

Fig. 3. Mean velocity profile of flying wire axial traverse, single-wire probe averaged over 20 runs.

Fig. 4. The base structure of the FHWS.

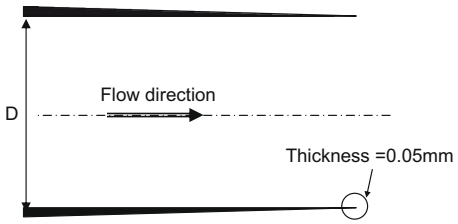

Fig. 5. Cross section of the nozzle at jet exit; $D = 8.25$ cm.

conditions and thus the present study was restricted to axial locations where effects of confined spaces are deemed small. The rig was originally constructed to investigate co-axial jet flow. Fig. 6 shows a schematic of the rig. In the present configuration, the outer co-flow was disabled and the nozzle that would produce the outer co-flow removed.

2.3. Field measurements and data processing

The experiments were carried out at three Reynolds numbers, based on the exit bulk velocity and the source diameter: 6000, 10,000 and 30,000. Measurements extend downstream along the jet axis to $x/D \approx 30$ and in the case of the stationary hot wire in the spanwise direction from $r/D = -12$ to $r/D = 12$.

Measurements of mean velocities and turbulence statistics were obtained using single and cross wires. A Dantec constant temperature anemometer (CTA) was used. The complete measuring system was composed of hot-wire probes, a Dantec streamline (CTA 90N10 Frame) with four modules, a 16-Analog-Input Multifunction DAQ card PCI-6052E (*333 kS/s, 16-Bit*), a National Instruments SCXI signal conditioning (containing a SCXI 1000 chassis, an 8-channel simultaneous-sampling differential amplifier module SCXI 1140 and a shielded terminal block with BNC connectors SCXI 1305) and a personal computer (Pentium 4 940 dual-core CPU with 36 GB internal hard drives and connected to a 6 TB hard drive array, configured as a RAID 5, via a 4 GB fibre channel controller). The SHW measurements were taken with a sampling frequency of 30 kHz for a total of 36×10^6 samples per measurement position (record length was 2 min). The flying hot-wire spatial resolution was 1.5×10^{-4} m. Thus over approximately 2.5 m of travel, and at a sampling rate of 30 kHz, produced 5×10^8 data points per traverse. In the current experiment, 300 traverses were used, which therefore provided 1.5×10^{11} data points (0.15 *tera-words*). These data were ensemble averaged to provide axial mean and turbulence intensity values at every $x/D = 0.5$ position.

The FHWS created an interesting "noise" problem. This was identified as an electromotive motive force (EMF) coupling between the Parker TD3 controller and the BNC connectors of the SCXI unit. The implementation of a Faraday-like cage (aluminum foil) around the SCXI unit helped, but eventually a low-pass filter and a cutoff frequency of 3500 Hz was applied to the data. The calculated velocity spectra confirmed that for the present set of measurements this filter had no effect on the reported results.

2.4. Hot-wire calibration

The probe was calibrated in the potential core of the jet, as its velocity field is uniform over the space occupied by the sensors and prong. The calibration was done before and after each experimental run. The velocity calibration range was 1–26 m/s. The flying hot wire was calibrated in the stationary mode as explained by Bruun [35].

For the single wire calibration, only the probe-stem is required to be aligned with the mean flow direction. For the cross-wire calibration, each wire has its own coordinate system. It was important to describe the sensitivity of the hot wire to variation in flow velocity and wire orientation. To transform the output voltage into a velocity component in a common probe–stem coordinate system, the method described in Westphal and Mehta [36] was used. Calibrations were done in two stages: the first was the "*static velocity response*" or "*King's law*", where the probe was aligned with the mean flow direction while a static calibration was performed. It was used to provide the relation between the effective cooling velocity and the bridge voltage output. In the second stage, a "*yaw-calibration procedure*" or "*cosine law*" was used to relate the

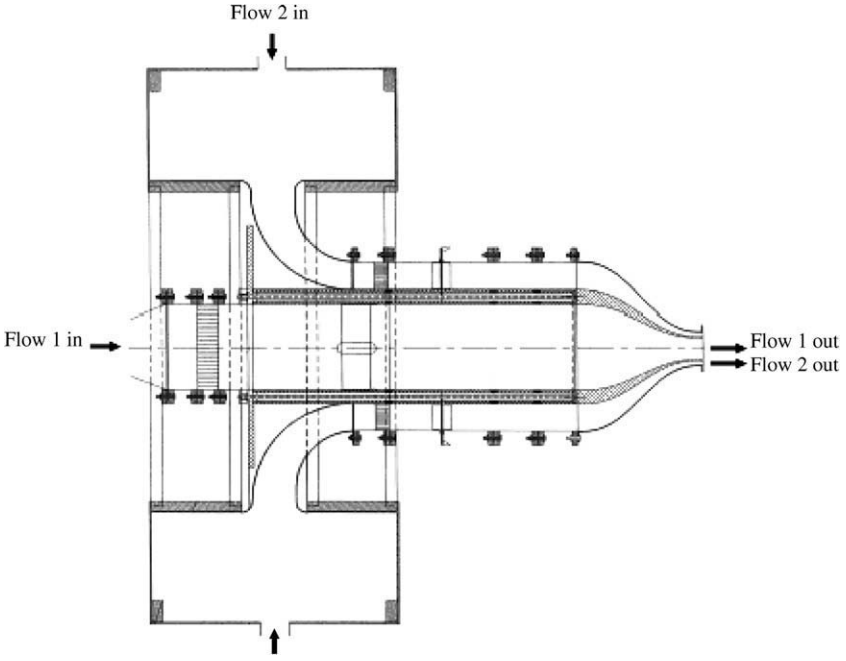

Fig. 6. The general flow rig. It is a jet co-flow rig and in the experiments reported here flow 2 is disabled and the outer nozzle that would contain flow 2 was removed, see Fig. 2.

effective cooling velocity to the magnitude and direction of the velocity vector. The free-stream velocity of the jet was held constant while the wires were inclined at various angles from the measurement orientation by rotating the wire by 5° in the yaw angles range ±40°.

2.5. System control and data acquisition

Control of the flying/stationary hot-wire system, which included positioning of the rake and data acquisition was accomplished using the National Instruments software LabVIEW (laboratory virtual instrumentation engineering workbench). For the positioning system (move motors, check velocities, accelerations, decelerations, homing, inputs and outputs), LabVIEW interfaces with the Parker Compumotor's 6K controller (multi-axis motion controller) using a 6K motion language (Parker Motion Planner) via a serial *Rs-232* cable.

3. Presentation and discussion of results

3.1. Initial conditions

The initial conditions were measured using the stationary hot wire at $x/D = 0.04$ for the three different Reynolds numbers considered. Profiles of axial mean velocity, axial and radial turbulence intensity and Reynolds stress are presented in Fig. 7. The axial mean velocity profile, Fig. 7a, indicate that the exit profile is insensitive to *Re*. Fig. 7b indicates that the axial turbulence intensity, which is less than 3%, increases with *Re*. A careful examination of this graph confirms that in the central portion of the jet the axial turbulence intensity decreases due to the increase in U_j while at $r/D = \pm 0.4$ the intensity reflects the thinning of the boundary layer at the nozzle exit with increased *Re*. For the Reynolds number of 30,000, the exit momentum thickness taken when $U = 0.99U_j$ was found to be $0.055D$. The boundary layer displacement was found to be equal to $0.058D$. These values are in good agreement with those of Mi et al. [19] that found the momentum and displacement thickness to be $0.047D$ and $0.063D$, respectively. The transverse turbulent intensity is less than 1%. The Reynolds shear stress distribution, Fig. 7d, vanishes on the centreline, as expected.

3.2. Flow evolution

Unless noted, those data presented are from the use of stationary hot wires.

The axial mean velocities, normalized by the centreline velocity, at different axial positions x/D, are presented in Fig. 8. The profiles are symmetric within measurement uncertainty. The 'top-hat' distribution at the nozzle exit tends to persist to about $5–6D$. The axial mean velocity profile at $x/D = 5$ and $Re_D = 6000$ is not as developed as for $Re_D = 10{,}000$ and 30,000, as it retains remnants of the initial conditions. This result is in agreement with the results of Weisgraber and Liepmann [37] for Reynolds numbers 5500 and 16,000.

The corresponding axial and transverse turbulence intensity profiles, for $0.04 < x/D < 15$ are displayed in Figs. 9 and 10, respectively. The axial and radial turbulence intensities have nearly the same shape. In general, the axial turbulence intensity, u'/U_c, is greater than the transverse turbulence intensity, v'/U_c, along the streamwise direction. At $x/D = 15$, the turbulence intensities are clearly anisotropic and the reason for which is likely due to

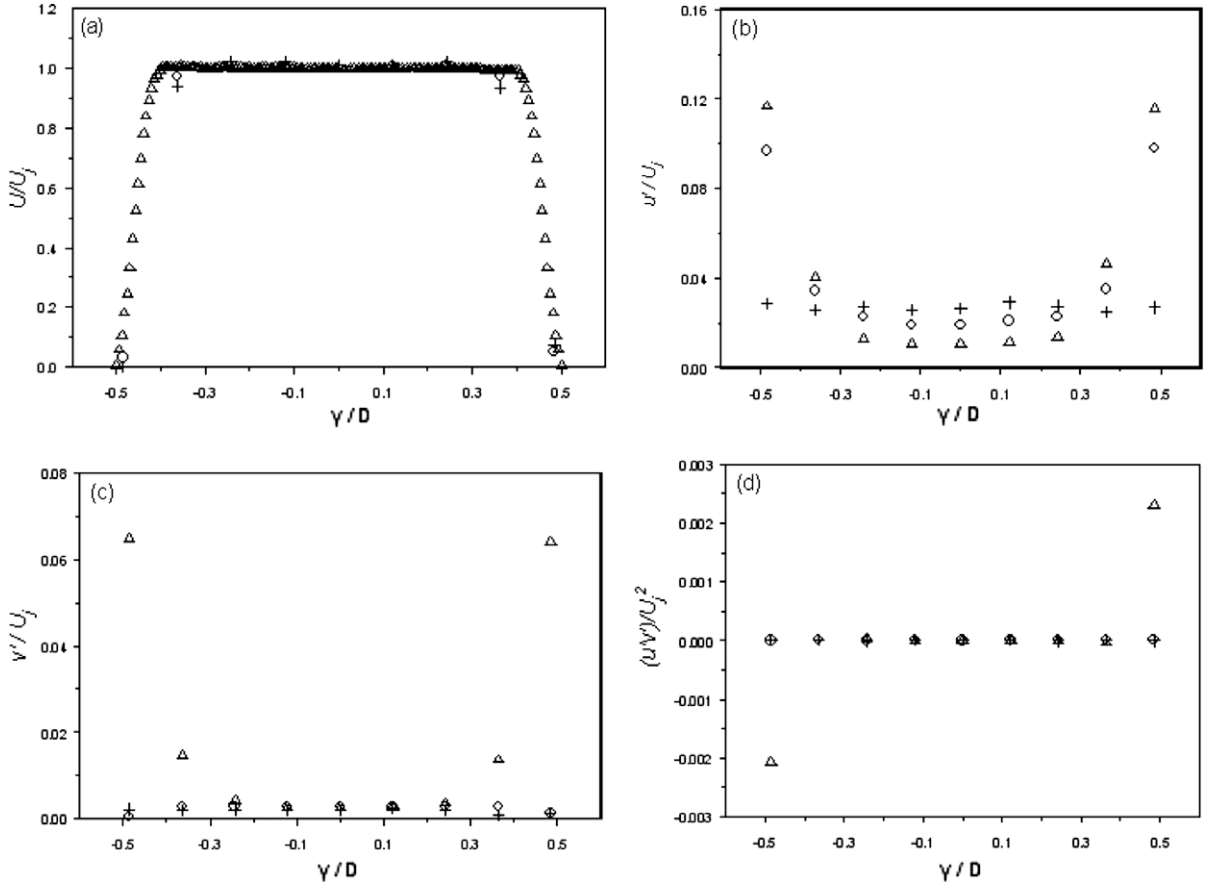

Fig. 7. Initial conditions at $x/D = 0.04$: (a) streamwise mean velocity; (b) u'/U_j; (c) v'/U_j; (d) $(u'v')/U_j^2$. Symbols: (△) $Re_D = 30{,}000$, (○) $Re_D = 10{,}000$, (+) $Re_D = 6000$.

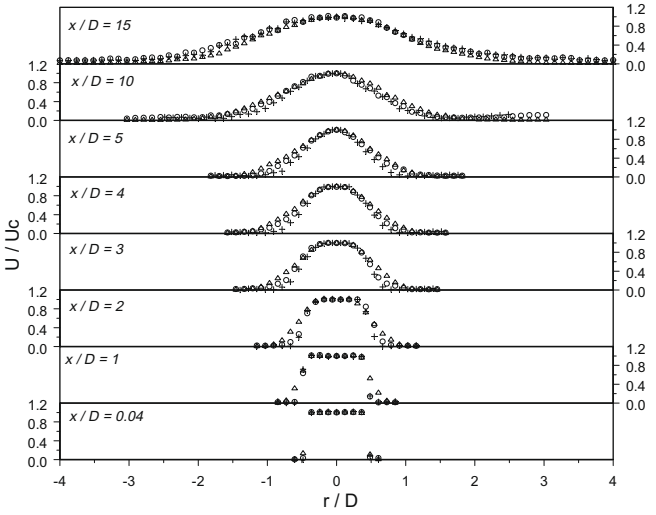

Fig. 8. Streamwise mean velocity at different axial positions. Symbols: (△) Re_D = 30,000, (○) Re_D = 10,000, (+) Re_D = 6000.

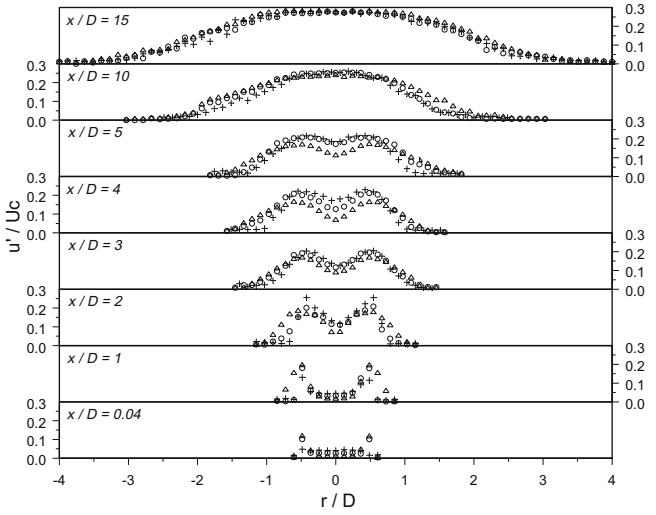

Fig. 9. Streamwise turbulence intensity at different positions. Symbols: (△) Re_D = 30,000, (○) Re_D = 10,000, (+) Re_D = 6000.

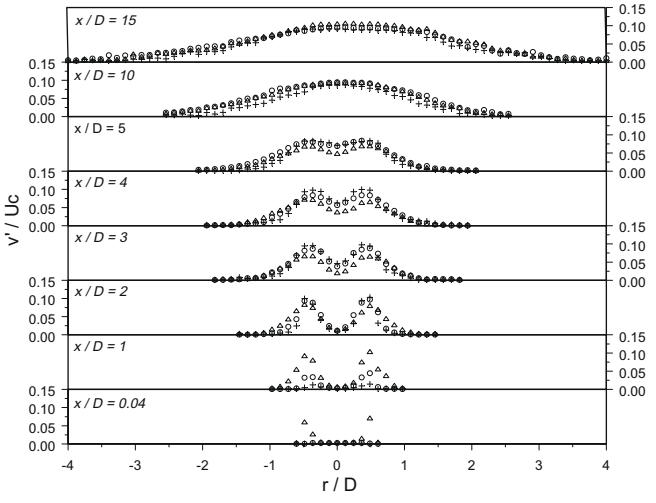

Fig. 10. Transverse turbulence intensity at different positions. Symbols: (△) Re_D = 30,000, (○) Re_D = 10,000, (+) Re_D = 6000.

turbulence structure influences as will be revisited below. One of the most interesting features of the NIF region is the way in which the turbulence intensities re-distribute across the jet as the flow evolves downstream. That said, at x/D = 15, the time averaged turbulence distributions are remarkably similar in their shape.

Fig. 11 presents the Reynolds shear stress, normalized by the square of the centreline velocity U_c^2. The greatest exchange of momentum, which involves large-scale vortices, occurs in the jet shear layer. The maximum Reynolds stress is shifted away from the jet centreline with increased downstream distance. Citriniti and George [38] used 138 synchronized channels of hot-wire anemometry, for Re_D = 80,000 and at x/D = 3 only and applied the proper orthogonal decomposition to reconstruct the global velocity field. From their data, they found that longitudinal counter-rotating vortices create alternating positive and negative radial fluid advection patterns. Clockwise positive vorticity is on the positive r/D side of the present jet. Citriniti and George [38] concluded that the life-cycle of the large-scale structures includes intra-vortex ring braids, which appear as counter-rotating pairs, and the intra-vortex region is a high strain field and that the braids are integral to the entrainment process. McIlwain and Pollard [5] confirmed this in an LES study of round jets with and with out swirl.

Figs. 8–11 reveal a close coupling between the mean velocity distribution and the turbulence intensity and Reynolds shear stress. The location of the peaks in the turbulence intensity profile corresponds to the local maximum of the mean velocity gradient. The Reynolds shear stress distribution is symmetrical, as expected. The mean velocity seems to evolve to the self-similar state (which is not reached in this study) more quickly than do the turbulence intensities. Wygnanski and Fiedler [7] claimed that a self-similar state is where all flow turbulence components are in equilibrium. However, since the energy is transferred from the mean motion directly to the fluctuating velocities so that similarity is approached in a series of intermediate steps. First, the axial mean velocity becomes self-similar, which leads to the production of u'-fluctuations, then the radial component v'-fluctuations reaches equilibrium. At x/D = 15, which is the last measurement station in the current stationary hot-wire experiment, the axial mean velocity is about 1/3 that at the jet exit ($U_j \sim 1.84$ for Re = 6000). Thus it is difficult to unequivocally state that the Reynolds stress profile takes longer to evolve into a fully developed state, for example. The Reynolds number effect is clearly visible in the near-field

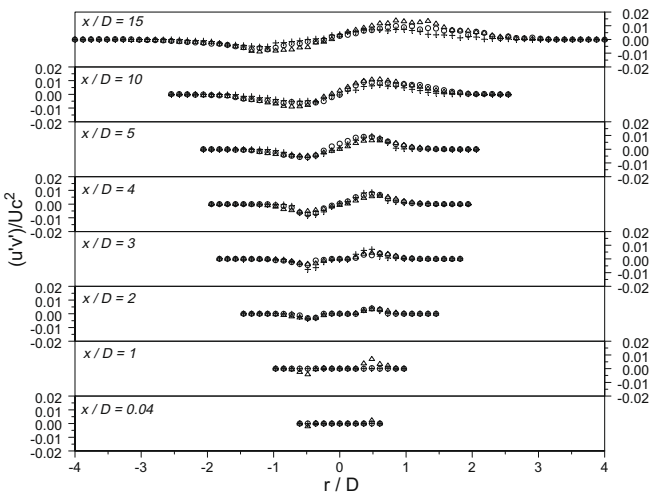

Fig. 11. Reynolds shear stress at different positions normalized using local axial mean velocity squared. Symbols: (△) Re_D = 30,000, (○) Re_D = 10,000, (+) Re_D = 6000.

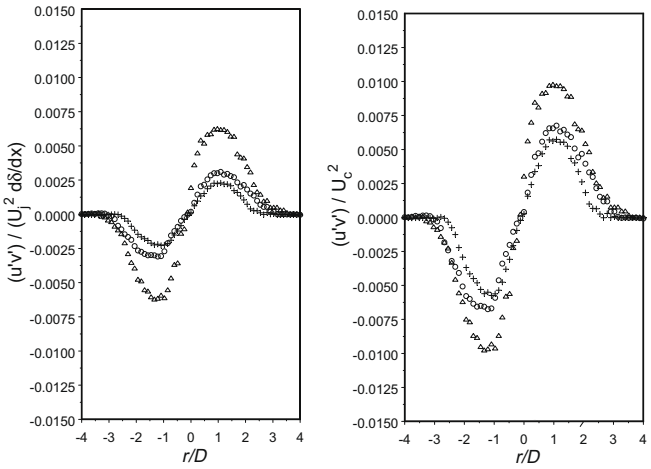

Fig. 12. Reynolds shear stress at $x/D = 15$ normalized left using George [9] and right using local axial mean velocity squared. Symbols: (△) $Re_D = 30{,}000$, (○) $Re_D = 10{,}000$, (+) $Re_D = 6000$.

portion of the shear layer. At $x/D = 15$, the Reynolds stress profile has been normalized using George's [9] suggested scaling of $U_j^2/(d\delta/dx)$, see Fig. 12. As expected, these results indicate that the flow is not fully developed in the region considered and so self-similarity cannot be expected.

Fig. 13 displays the axial mean velocity decay obtained using both a stationary and flying hot wire. Fig. 13 demonstrates that in the near-field region ($x/D < 6$) there is no significant variation in the centreline axial mean velocity with Reynolds number. The centreline axial mean velocity decays linearly with axial distance. Beyond the potential core, the influence of initial condition is not apparent. The variation of the mean centreline velocity downstream of the jet exit is independent of the Reynolds number, which is in agreement with the result of Suresh et al. [39] and Mi et al. [19]. For a self-similar jet, the centreline velocity variation is given by:

$$\frac{U_j}{U_c} = \frac{1}{B}\left(\frac{x}{D} - \frac{x_0}{D}\right) \tag{2}$$

where x_0 is the virtual origin and B is the decay constant. Table 1 provides values for these quantities for the present results and also

Table 1
Centreline mean velocity parameters, see Eq. (2).

Authors	x/D	x_0/D	B
Present study	15–29	2.5	5.59
Wygnanski and Fiedler [7]	<50	3	5.7
	>50	7	5.0
Panchapakesan and Lumley [11]	30–160	0	6.06
Hussein et al. [13]	30–120	2.7	5.9
Ferdman et al. [18]	⩾15	2.5	6.7
Mi et al. [19]	0–64	3.5	4.48
Weisgraber and Liepmann [37]	17–27	0	6.7
Xu and Antonia [40]	20–75	3.7	5.6
Quinn [41]	18–55	2.15	5.99

those obtained from the literature. Good agreement is found. It appears that in the intermediate-field region, the centreline velocity decays faster than in the self-similar region due to the flow development. Note that on Fig. 13, the solid line drawn between $x/D \sim 14$ and $x/D \sim 28$ fits the mean of both the flying and stationary hot-wire data and the error bars indicate ±0.05 U_j/U_c, where the subscripts j and c refer to the jet exit and the local axial centreline values. It is clear that for the axial mean velocity, the stationary and flying hot-wire data are the same within experimental uncertainty, including possible sampling limitations with the flying hot wire (that is, only 300 data points were acquired at each axial location as compared to the 3.6 million for each position for the stationary hot wire).

The longitudinal evolution of the turbulence intensities obtained from the stationary and the flying hot wire along the jet axis ($r/D = 0$) and for the stationary hot wire along a line of constant radius ($r/D = 1/2$) is provided in Fig. 14. Fig. 14 there are plotted data from Xu and Antonia [40], Abdel-Rahman et al. [42] and Tong and Warhaft [43] for Reynolds numbers below and above the mixing transition. The FHW data are seen to be in excellent agreement with the SHW data; the slight disparity between the two sets of data at axial distances $x/D > 15$ is probably due to insufficient sampling in the case of the FHWS. Panchapakesan and Lumly [11] for example used 1000 runs to ensemble average their data (taken between $30 < x/D < 120$). The present results are in good agreement with those of Xu and Antonia [40], Abdel-Rahman et al. [42] and Tong and Warhaft [43]. In the near-field region, the turbulence intensities increase due to the large-scale coherent motions that

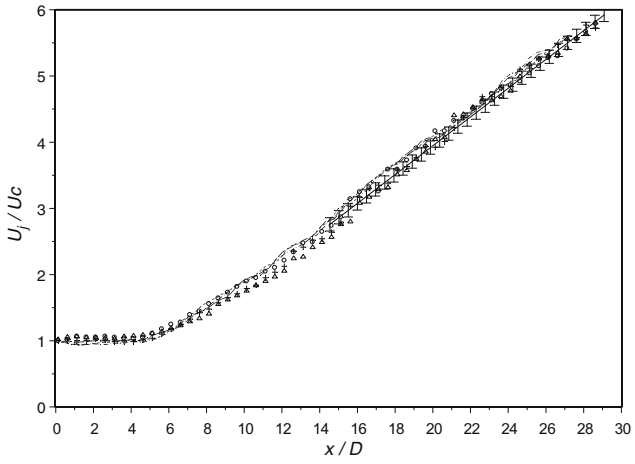

Fig. 13. Axial decay of centreline mean velocity. —— Line drawn to indicate mean of the data equal to $1/x$ SHW measurements: (△) $Re_D = 30{,}000$, (○) $Re = 10{,}000$, (+) $Re = 6000$, FHW measurements: — — — $Re_D = 30{,}000$ ····· $Re_D = 10{,}000$, — • — $Re_D = 6000$.

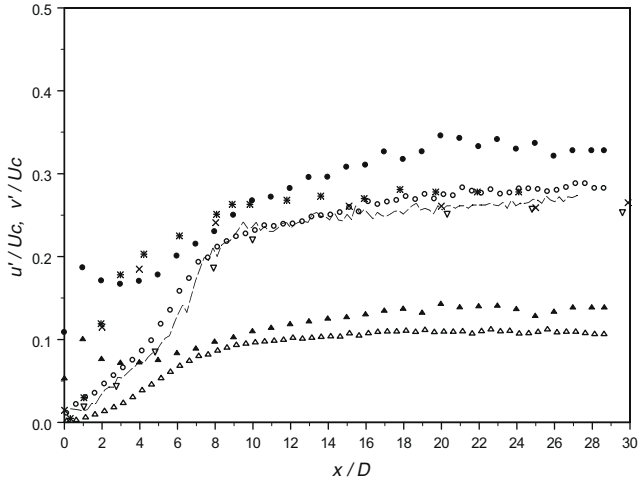

Fig. 14. Evolution of centreline turbulence intensities at $Re_D = 30{,}000$. Symbols: (○) u'/U_c, (△) v'/U_c. FHW measurements: — — —, (▽) u'/U_c at $Re_D = 86{,}000$ (Xu and Antonia [40]), (×) u'/U_c at $Re_D = 13{,}200$ (Abdel-Rahman et al. [42]), (∗) u'/U_c at $Re_D = 140{,}000$ (Tong and Warhaft [43]),no-filled symbols: $r/D = 0$, filled symbols: $r/D = 1/2$.

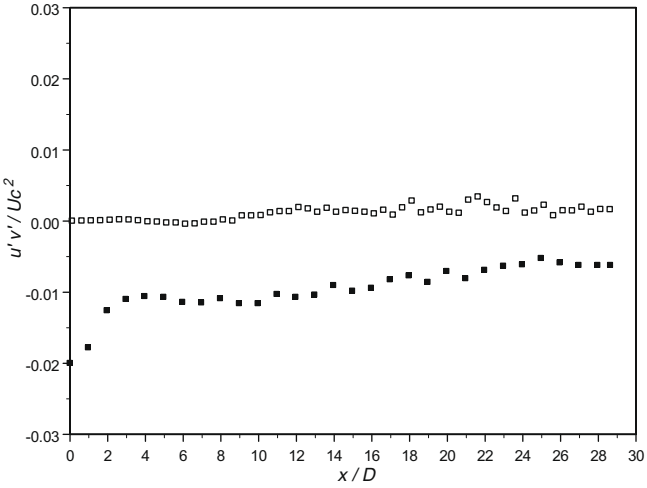

Fig. 15. Evolution of Reynolds shear stress at $Re_D = 30{,}000$. No-filled symbol: $r/D = 0$, filled symbol: $r/D = 1/2$.

arise in the shear layer and their influence on the centreline intensities increases as they progress through the potential core and eventually coalesce at the end of the potential core and then mix as the flow develops towards equilibrium in the far-field. The intensities reach the nominally accepted value of about 28% at $x/D = 30$, Wygnanski and Fiedler [7]. The turbulence intensities in the shear layer are higher than at the centreline because the mixing layer generates highly energetic large turbulent structures, which are confirmed by the Reynolds shear stress, as presented in Fig. 15. The evolution of the structures close to the nozzle exit at $r/D = 1/2$ is due to the initial shear layer instabilities, of the Kelvin–Helmholtz type, which break down into vortical structures with kinetic energies of the order of the mean flow in the layer (Ferdman et al. [18] and Hussain and Clark [44]). Immediately downstream of the nozzle exit (recall that the nozzle exit is razor-sharp with land thickness of 0.05 mm), the initial turbulence energy decays before it increases again at about $3D$ under the effect of the growing large structures that originate from the roll-up in the shear layer. When the initial shear layer becomes unstable, velocity fluctuations increase in amplitude, which result in the roll-up of the shear layer into a train of azimuthally oriented vortex elements which pair-up to form large vortical structures and this occurs for any slight asymmetry in the spacing of two adjacent vortices, or inequality in their strengths (Mi et al. [19]). The turbulence intensities in the shear layer ($r/D = 1/2$) are similar in shape to those observed by Burattini et al. [26] for the case of the flow downstream the grids placed at the nozzle exit plane and taken along the jet centreline. The use of grids obviously introduce more or less incoherent vorticity into the potential core of the jet without significantly affecting the formation of Kelvin–Helmholtz type instabilities; that is the jet remains convectively unstable, see Fiedler [4] for example. Moreover, the introduction of grids at the jet exit suggests that the velocity spectral content of the flow in these two cases should also be similar. It is to the velocity spectra that attention is now turned.

Figs. 16 and 17 show, respectively, the axial and transverse velocity spectra (Eq. (3)) which were calculated from data gathered at various x/D and for $r/D = 0$ and $1/2$.

The one dimensional energy spectrum, $E_{ii}(f)$, may be defined by:

$$E_{ii}(f) = \int_{-\infty}^{+\infty} e^{-i(2\pi f)\tau} R_{ii}(\tau) d\tau \tag{3}$$

where $R_{ii}(\tau)$ is the autocorrelation defined as:

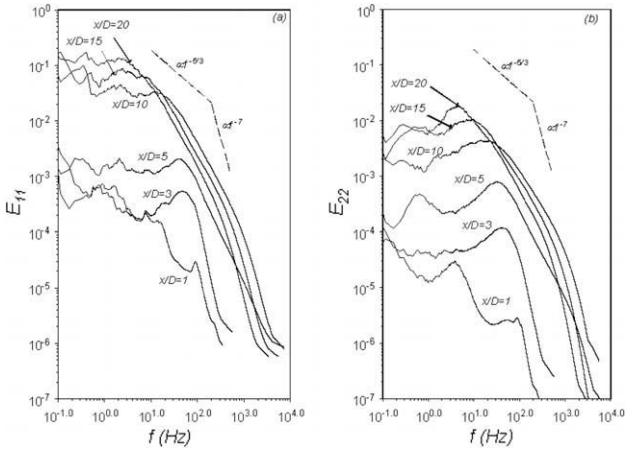

Fig. 16. Velocity spectra at $r/D = 0$ and $Re_D = 30{,}000$ at various x/D locations: (a) u-spectra; (b) v-spectra.

$$R_{ii}(\tau) = \int_{-\infty}^{+\infty} u_i(\tau + t) u_i(\tau) d\tau = \overline{u_i(\tau + t) u_i(\tau)} \tag{4}$$

where $R_{11}(\tau) = \overline{u(\tau + t) u(\tau)}$, $R_{22}(\tau) = \overline{v(\tau + t) v(\tau)}$

The dotted-lines in these figures correspond to $f^{-5/3}$ and f^{-7} have also been included. In turbulent flows, the $-5/3$ slope is associated with the range of frequencies in which the energy cascade is dominated by inertial transfer, i.e., Taylor's frozen field hypothesis is applicable, while the f^{-7} slope characterizes the dissipation range where viscous forces dominate. Consider the jet axis ($r/D = 0$) at $x/D = 1$ and 3. The turbulence intensity is the lowest and the mean velocity is the highest at these locations and the velocity spectra display different shapes with local peaks that reflect the exit conditions. At these positions, the formation of coherent structures is apparent with the increased energy content at between 60 and 100 Hz. Within the shear layer region ($r/D = 1/2$), at the same positions $x/D = 1$ and 3, these peaks disappear and the velocity spectra evolve to what is expected for more fully developed turbulence and display the $-5/3$ and -7 slopes. Farther downstream ($x/D = 10$–20), for both cases, $r/D = 0$ and $1/2$, the velocity spectra continue to develop and display frequency ranges over many decades. In both the inertial sub-range and dissipation range, for both cases, $r/D > 0$ and $1/2$, the low frequency components of the velocity spectra increase with increased axial distance while the high

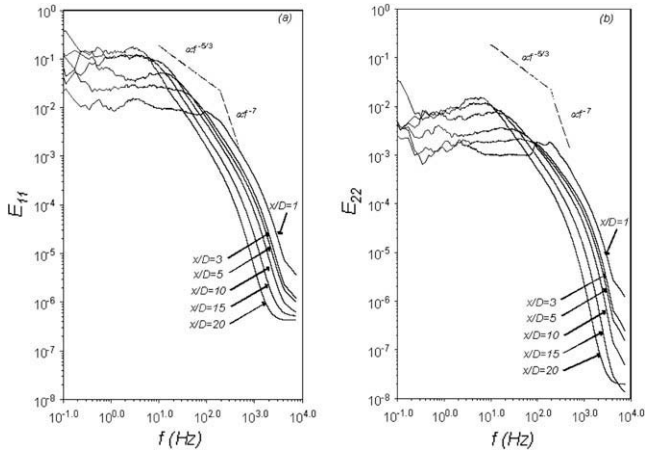

Fig. 17. Velocity spectra at $r/D = 1/2$ and $Re_D = 30{,}000$ at various x/D locations: (a) u-spectra; (b) v-spectra.

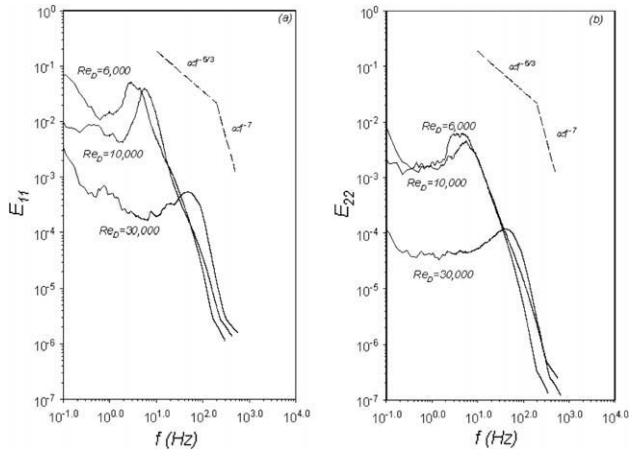

Fig. 18. Velocity spectra at $r/D = 0$ at $x/D = 3$ at $Re_D = 6000$, 10,000 and 30,000: (a) u-spectra; (b) v-spectra.

frequency components decrease in frequency. Note, however, that when plotted using the normalized one dimensional energy spectrum function $(E_{11}(\kappa 1)/(\eta u_\eta{}^2)$ *vs.* $(\kappa_1\eta)$, these Kolomogorov-based velocity spectra- collapse in the inertial sub-range higher frequencies for axial distances beyond the potential core, see Fellouah and Pollard [45]. In general, the evolution of the velocity spectra is in agreement with those data from Burattini et al. [26]. The velocity spectra are also in agreement with those of Jung et al. [25] who used SHW in an axisymmetric turbulent jet between $2 < x/D < 6$.

Figs. 18 and 19 provide the velocity spectra on the jet centreline for two axial locations, $x/D = 3$ and 10, and for the three Reynolds numbers considered. It is clear that the mixing transition, which demarcates $Re = 10{,}000$ and $Re = 30{,}000$, display very different velocity spectral energy content, most noticeably at $x/D = 10$. The inertial sub-range is certainly evident at $Re = 30{,}000$ than at the lower Reynolds numbers, while the dissipation range is in greater evidence for the lower, sub-mixing transition Reynolds numbers. Dimotakis [2] argues that the mixing transition should occur when there is a separation between the large and viscous scales and free from viscous effects; that is between the inertial sub-range and the dissipation range. Based upon those data presented here, it is the appearance on the inertial sub-range itself that may indicate the mixing transition.

There is a growing body of literature that indicates the sensitivity of turbulence to inlet conditions, see for example Slessor et al. [46] and George [9]. However, in those data presented here, data were taken using the same experimental rig, the same experimental conditions (save for altering the inlet Re) and equipment and experimentalist, so it is believed the effects of altering the inlet Re are a direct result of the change in Re only. Additionally, in the case of a planar mixing layer, Huang and Ho [47] provide an interesting link to the formation of the $-5/3$ region through vortex merging.

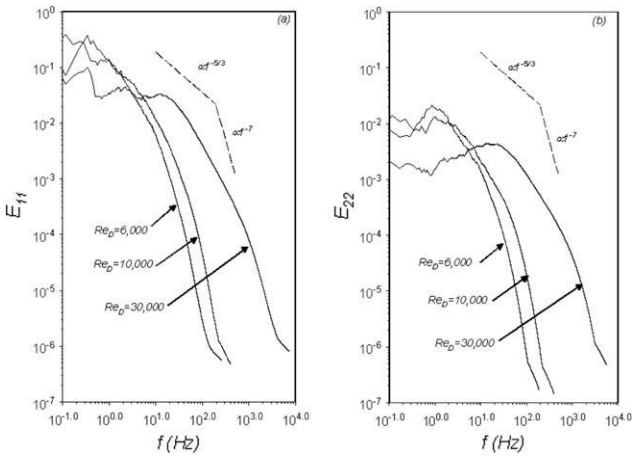

Fig. 19. Velocity spectra at $r/D = 0$ at $x/D = 10$ for $Re_D = 6000$, 10,000 and 30,000: (a) u-spectra; (b) v-spectra.

4. Conclusion

In the present paper we have explored experimentally the effect of the Reynolds number on the near- and intermediate-fields $(0 \leqslant x/D \leqslant 25)$ of an axisymmetric round free jet, using stationary and flying hot-wire anemometry. Data have been presented for the axial mean velocity profiles, turbulence intensities and velocity spectra. Results reveal a close coupling between the mean velocity distribution and the turbulence intensities and the Reynolds shear stress. The effect of the Reynolds number depends on the region of the jet considered. In the shear layer region, where the moments are higher, its effects can be seen more clearly. The length of the potential core region decreases with increasing Reynolds number. At the nozzle exit, the boundary layer thickness decreases slightly with the Reynolds number. In the near-field, the downstream variation of the mean centreline velocity is independent of the Reynolds number. As the jet evolves downstream, the axial mean velocity evolves faster to the self-similar state than the turbulence intensities and the streamwise turbulence intensity was greater than the transverse turbulence intensity. The increase of the radial development of the jet downstream was visible in the Reynolds stress results, where its maximum was shifted away from the jet centreline.

From the data obtained, it was shown that with the downstream evolution of the jet, the range of the frequencies that comprise the inertial sub-range increases and the intensity of the velocity spectra decreases in both the inertial sub-range and in the dissipation range. The Reynolds number range considered in this study clearly points to a mixing transition and for Reynolds numbers above ~20,000, the velocity spectra were accompanied by the appearance of the inertial sub-range. At Reynolds numbers below the mixing transition, the energy of the large scale turbulence (low wavenumbers or frequencies) proceeds directly to the dissipation range (-7 slope in the frequency spectra).

The limited data obtained with the flying hot wire confirms that the experimental methodology accords with usual stationary wire approaches.

Acknowledgments

This work was supported financially by the Natural Sciences and Engineering Research Council (NSERC, Canada) through Discovery Grants (DG) program and equipment grants. The authors wish to thank Dr. Dan Ewing for the original design and construction of the co-flowing jet rig, Mr. C.G. Ball for initial work on developing the flying hot-wire rig and to Professor Mark Glauser, Syracuse University for advice on FHW systems. Professor Paul Dimotakis kindly provided the reference to the mixing layer literature. And finally, to Professor D.B. Spalding for his mentorship, friendship and inspired thinking and creativity that continues to inspire this former student (AP) and then in turn to DBS' academic grandchildren.

References

[1] F. Ricou, D.B. Spalding, Measurements of entrainment by axisymmetric turbulent jets, J. Fluid Mech. 11 (1961) 21–32.

[2] P.E. Dimotakis, The mixing transition in turbulent flows, J. Fluid Mech. 409 (2000) 69–98.
[3] C. Benocci, S. Tavoularis, J.-P. Bonnet, O. Leuciter, W. Rodi, M. Onorato, h.J.J.W. Van der Vegt, J. Jimenez, P.D. Smith, B. Cantwell, R.S. Moser, L.P. Purtell, A Selection of Test Cases for the Validation of Large Eddy Simulations of Turbulent Flows, NATO AGARD-AR-345, 1988.
[4] H.E. Fiedler, Control of free turbulent shear flows, in: M.G. El-Hak, A. Pollard, J.P. Bonnet (Eds.), Flow Control: Fundamentals and Practices, Springer-Verlag, Germany, 1998, pp. 335–429.
[5] S. Mcllwain, A. Pollard, Large eddy simulation of the effects of mild swirl on the near field of a round free jet, Phys. Fluids 14 (2) (2002) 653–661.
[6] C.G. Ball, A. Pollard, A review of experimental and computational studies of flow from the round jet, Internal Report: Department of Mechanical and Materials Engineering, Queen's University, 2008.
[7] I. Wygnanski, H. Fiedler, Some measurements in the self-preserving jet, J. Fluid Mech. 38 (1969) 577–612.
[8] W. Rodi, A new method of analysing hot-wire signals in highly turbulent flow and its evaluation in a round jet, DISA Inf. 17 (1975).
[9] W.K. George, The self-preservation of turbulent flows and its relation to initial conditions and coherent structures, in: W.K. George, R. Arndt (Eds.), Advances in Turbulence, Springer Verlag, New York, 1989, pp. 39–73.
[10] D.R. Dowling, P.E. Dimotakis, Similarity of the concentration field of gas-phase turbulent jets, J. Fluid Mech. 218 (1990) 109–141.
[11] N.R. Panchapakesan, J.L. Lumley, Turbulence measurements in axisymmetric jets of air and helium. Part 1: air jet, J. Fluid Mech. 246 (1993) 197–223.
[12] C.D.D. Richards, W.M. Pitts, Global density effects on the self-preservation behaviour of turbulent free jets, J. Fluid Mech. 254 (1993) 417–435.
[13] H.J. Hussein, S. Capp, W.K. George, Velocity measurements in a high-Reynolds number, momentum-conserving, axisymmetric, turbulent jet, J. Fluid Mech. 258 (1994) 31–75.
[14] M. Uddin, A. Pollard, Self-similarity of co-flowing jets: the virtual origin, Phys. Fluids 19 (6) (2007) 68103/1–68103/4.
[15] W.M. Pitts, Reynolds number effects on the centreline mixing behavior of axisymetric turbulent jets, Exp. Fluids 11 (1991) 135–144.
[16] R.A. Antonia, Q. Zhao, Effect of initial conditions on a circular jet, Exp. Fluids 31 (2001) 319–323.
[17] B.J. Boersma, G. Brethouwer, F.T.M. Nieuwstadt, A numerical investigation on the effect of inflow conditions on the self-similar region of a round jet, Phys. Fluids 10 (4) (1998) 899–909.
[18] E. Ferdman, M.V. Otugen, S. Kim, Effect of initial velocity profile on the development of the round jet, J. Propul. Power 16 (4) (2000) 676–686.
[19] J. Mi, D.S. Nobes, G.J. Nathan, Influence of jet exit conditions on the passive scalar field of an axisymmetric free jet, J. Fluid Mech. 432 (2001) 91–125.
[20] G.P. Romano, R.A. Antonia, Longitudinal and transverse structure functions in a turbulent round jet: effect of initial conditions and Reynolds number, J. Fluid Mech. 436 (2001) 231–248.
[21] T. Matsuda, J. Sakakibara, On the vortical structure in a round jet, Phys. Fluids 17 (2005) 1–11.
[22] G. Carazzo, E. Kaminski, S. Tait, The route to self-similarity in turbulent jets and plumes, J. Fluid Mech. 547 (2006) 137–148.
[23] A.K.M.F. Hussain, K.B.M.Q. Zaman, The 'preferred mode' of the axisymmetric jet, J. Fluid Mech. 110 (1981) 39–71.
[24] M. Olsson, L. Fuchs, Large eddy simulation of the proximal region of a spatially developing circular jet, Phys. Fluids 8 (8) (1996) 2125–2137.
[25] D. Jung, S. Gamard, W.K. George, Downstream evolution of the most energetic modes in a turbulent axisymmetric jet at high Reynolds number. Part 1: the near-field region, J. Fluid Mech. 514 (2004) 173–204.
[26] P. Burattini, R.A. Antonia, S. Rajagopalan, M. Stephens, Effect of initial conditions on the near-field development of a round jet, Exp. Fluids 37 (2004) 56–64.
[27] S.J. Kwon, I.W. Seo, Reynolds number effects on the behaviour of a non-buoyant round jet, Exp. Fluids 38 (2005) 801–812.
[28] C. Bogey, C. Bailly, Large eddy simulations of transitional round jets: influence of the Reynolds number on flow development and energy dissipation, Phys. Fluids 18 (2006) 1–14.
[29] P.D. Beuther, A. Shabbir, W.K. George, X-wire response in turbulent flows of high intensity turbulence and low mean velocities, American Society of Mechanical Engineers, Fluids Eng. Div. 53 (1987) 39–42.
[30] B.J. Cantwell, A flying hot-wire study of the turbulent near wake of a circular cylinder at a Reynolds number of 140 000, Ph.D. thesis, California Institute of Technology, 1976.
[31] J.H. Watmuff, A.E. Perry, M.S. Chong, A flying hot wire system, Exp. Fluids 1 (1983) 63–71.
[32] B.E. Thompson, J.H. Whitelaw, Flying hot-wire anemometry, Exp. Fluids 2 (1984) 47–55.
[33] D.R. Cole, M.N. Glauser, Flying hot-wire measurements in an axisymetric sudden expansion, Exp. Therm. Fluid Sci. 18 (1998) 150–167.
[34] T. Morel, Design of 2-dimensional wind tunnel contractions, J. Fluids Eng. Trans. ASME 99 (2) (1977) 371–378.
[35] H.H. Bruun, Hot-Wire Anemometry: Principles and Signal Analysis, Oxford University Press Inc., New York, 1995.
[36] R.V. Westphal, R.D. Mehta, Crossed hot-wire data acquisition and reduction system, NASA Technical Memorandum 85871, 1984.
[37] T.H. Weisgraber, D. Liepman, Turbulent structure during transition to self-similarity in a round jet, Exp. Fluids 24 (1998) 210–224.
[38] J.H. Citriniti, W.K. George, Reconstruction of the global velocity field in the axisymmetric mixing layer utilizing the proper orthogonal decomposition, J. Fluid Mech. 418 (2000) 137–166.
[39] P.R. Suresh, S.K. Das, T. Sundararajan, Influence of Reynolds number on the evolution of a plane air jet issuing from a slit, J. Fluids Eng. Trans. ASME 129 (2007) 1288–1296.
[40] G. Xu, R.A. Antonia, Effect of different initial conditions on a turbulent round free jet, Exp. Fluids 33 (2002) 677–683.
[41] W.R. Quinn, Upstream nozzle shaping effects on near field flow in round turbulent free jets, Eur. J. Mech. B Fluids 25 (2006) 279–301.
[42] A.A. Abdel-Rahman, W. Chakroun, S.F. Al-Fahed, LDA measurements in the turbulent round jet, Mech. Res. Commun. 24 (3) (1997) 277–288.
[43] C. Tong, Z. Warhaft, Turbulence suppression in a jet by means of a fine ring, Phys. Fluids 6 (l) (1994) 328–333.
[44] A.K.M.F. Hussain, A.R. Clark, Upstream influence on the near field of a plane turbulent jet, Phys. Fluids 20 (9) (1977) 1416–1426.
[45] H. Fellouah, A. Pollard, Velocity spectra in the development region of a round, free, turbulent jet, submitted for publication, Phys. Fluids (2009) (December).
[46] M.D. Slessor, C.L. Bond, P.E. Dimotakis, Turbulent shear-layer mixing at high Reynolds numbers: effects of inflow conditions, J. Fluid Mech. 376 (1998) 15–138.
[47] L.S. Huang, C.M. Ho, Small scale transition in a plane mixing layer, J. Fluid Mech. 210 (1990) 475–500.